JOURNAL OF SPACECRAFT AND ROCKETS
Vol. 57, No. 2, March–April 2020

Mars 2020 Wind Velocity Measurement Interferences at High Reynolds Numbers

Adelaida Garcia-Magariño,* Suthyvann Sor,† Rafael Bardera,‡ and Javier Muñoz§
National Institute of Aerospace Technology, 28850 Madrid, Spain

https://doi.org/10.2514/1.A34591

The Mars Environmental Dynamics Analyzer will be dedicated to getting meteorological data from Mars during NASA's Mars 2020 rover mission. High-quality Mars atmosphere measurements are required in order to build mathematical models of the climate on a planetary scale. The Mars 2020 rover will be equipped with two wind sensors installed on two separated booms working in active redundancy but producing a mutual aerodynamic interference on one another's wind measurements. This paper presents a systematic study on the interferences produced by the sensors and the rover body itself when measuring wind velocities in order to get insight to assess the uncertainties produced by this effect.

Nomenclature

L	=	characteristic length
L_{fs}	=	full-scale length
L_m	=	model length
P	=	pressure
Re	=	Reynolds number
Re_{fs}	=	full-scale Reynolds number
Re_m	=	model Reynolds number
$\tilde{u}$	=	dimensionless longitudinal velocity
V	=	characteristic velocity
V_{fs}	=	full-scale velocity
V_m	=	model velocity
$\tilde{v}$	=	dimensionless transversal velocity
β	=	wind direction
λ_L	=	length scale ratio
λ_V	=	velocity scale ratio
λ_ν	=	kinematic scale ratio
μ	=	dynamic viscosity
ν	=	kinematic viscosity
ν_{fs}	=	full-scale kinematic viscosity
ν_m	=	model kinematic viscosity
ρ	=	density

Subscripts

fs	=	full scale
m	=	model

I. Introduction

DUST is lifted in the Martian atmosphere due to many processes: one of them being the development of dust devils. Dust devils are particle-loaded vertical convective vortices characterized by high rotating wind speeds, as well as reduced pressure and increased temperature at their centers. Fitting dust devil action into the Martian global dust is problematic [1]. A recent heuristic model of dust-devil trajectories, which is able to simulate pressure and winds for a different model of vortices developed by Lorentz [2], requires available wind data with high enough quality. Hueso et al. [3] used the new Mars Environmental Dynamics Analyzer (MEDA) system to obtain such data. Mars wind data are also important in other geophysical phenomena, such as carving intracrater layered deposits [4], changes on dunes [5], or any other aeolian processes due to the wind-driven particle mobility [6]. In this context, Day et al. [4] studied transport models to explain how mounds could be carved by wind. Hansen et al. [5] studied the wind and CO_2 as possible agents of change on Mars's northern dunes. Wind-related features and processes observed in the Gusev crater by the Mars Exploration Rover named Spirit were presented in Ref. [7].

The Curiosity rover, on the other hand, visited the Bagnold dune field to understand current winds and aeolian processes [8]. Wind-driven particles in Mars were also studied in the work of Sullivan et al. [6]. Finally, another field of interest for which the wind velocities in Mars have relevance includes wind-driven rovers for planetary exploration. For a long-term planetary surface mission, there appears to be a need for the use of in situ propulsion; and the wind-driven rovers' concept, such as tumbleweed, has arisen as a valid solution [9].

Previous missions to explore Mars have carried wind sensors to measure the wind velocity and its direction in the Mars surface. The Viking Meteorology Instrument System, described in Ref. [10], incorporated two wind sensors based on a hot-film sensor; and they were mounted at 90 deg from each other. Additionally, a quadrant sensor was included to solve the wind direction ambiguity [11–13]. The Mars Pathfinder lander incorporated a meteorology instrument (Atmospheric Structure Instrument/Meteorology Package) to measure, among other parameters, the wind speed and direction at a height of 1.1 m. The wind sensor was on the top of a mast and consisted of six identical hot-wire anemometer elements. Additional details of the wind sensor can be found in Ref. [14]. A hot film anemometer for the Martian atmosphere, described by Dominguez et al. in Ref. [14], was on-board on the Mars Science Laboratory (MSL) Curiosity rover [15] as part of the Rover Environmental Monitoring System (REMS). The results of wind characterization on the Gale surface crater on Mars, based on measurements taken by the REMS, was recently presented by Viúdez-Moreiras et al. [16].

The Mars 2020 mission would be dedicated to the investigation of the environmental factors in the Martian atmosphere, among others. Spain contributed to the Mars 2020 Rover with the MEDA system: particularly, with the design of the two wind sensors on-board. The new wind sensors are based on hot film anemometry [14,15,17] because it is a very robust technology, as demonstrated during NASA's Viking mission [11–13]. The two wind sensors are located in a mast that supports a remote camera; due to the restrictions imposed by the design of the rover, wind measurements will be affected by the presence of its body (see Fig. 1 for the location of the booms). Previous studies carried out by Bardera et al. were

Received 15 July 2019; revision received 21 October 2019; accepted for publication 18 November 2019; published online 27 December 2019.

*Aerospace Engineer, Experimental Aerodynamic Branch, Torrejón de Ardoz; garciamga@inta.es.

†Aerospace Engineer, Experimental Aerodynamic Branch, Torrejón de Ardoz; sors@inta.es.

‡Aerospace Engineer, Experimental Aerodynamic Branch, Torrejón de Ardoz; barderar@inta.es.

§Aerospace Engineer, Experimental Aerodynamic Branch, Torrejón de Ardoz; munozcj@inta.es.

dedicated to this [18,19]. In the first work of Bardera et al. [18], experimental and numerical characterizations of the flow around the Mars 2020 Rover were presented. In that work, only vertical planes that passed through the vertical mast were investigated. Particle image velocimetry (PIV) measurements were obtained and compared to numerical simulations, showing good agreement, except for the detached regions. A 1/10th-scaled model was used with a wind-tunnel air speed of 20 m/s, leading to a Reynolds number of $2.4 \cdot 10^5$, and corresponding to the maximum velocity encountered in Mars. In the second work of Bardera et al. [19], the lowest Reynolds number expected in the Mars conditions ($Re = 6770$) was investigated. A 1/45th-scaled model was placed inside a low-velocity wind tunnel especially designed to obtain velocities of 2.5 m/s. Laser Doppler velocimetry (LDV) was used to obtain the three components of the velocity near the wind sensors. However, the rover model did not include the booms in order to use the LDV measurement technique. A method was proposed to calculate a correction factor for wind measurements obtained by the sensors on-board on rovers.

In the present work, the maximum expected Reynolds number will once again be investigated. Because previous works only showed the vertical planes, in this investigation, the horizontal influence on the wind sensors measurements will be studied and the errors that could be induced by the interference of the booms on one another will be evaluated. A 1/5th-scaled model will be used instead of the 1/10th one used in previous studies in order to gain resolution in the measurements near the boom. To obtain the same Reynolds number, the freestream wind-tunnel velocity has been reduced to 10 m/s.

First, the Mars 2020 Rover is briefly introduced; after that, the description of the experimental setup and the validity of the wind-tunnel experiments are presented; afterward, the experimental configurations tested are shown. The results and the discussion will follow, showing both the PIV velocities map at each yaw angle studied and the influence between booms. Finally, the conclusions are given.

II. Mars 2020 Rover

The main objective of the Mars 2020 mission is the exploration of the Martian surface by means of a new rover vehicle. A set of scientific instruments installed on board the rover will be transported around the surface of Mars as a mobile laboratory. The vehicle itself consists of a rectangular body supported by six wheels. The vertical mast supports a camera and the environmental instruments constituting the Mars Environmental Dynamic Analyzer. The power is supplied by the multimission radioisotope thermoelectric generator (MMRTG), which is located in the rear end of the body; it transforms the nuclear power of plutonium to electric power to be used by instruments and for the propulsion of the rover. A scheme of the vehicle can be observed in Fig. 1, where wind sensors of the MEDA are installed on both booms: 1 and 2. A robotic arm (not represented for simplicity) will be used to extract geological samples of Martian rocks to be analyzed by the scientific instruments housed inside the central body of the rover.

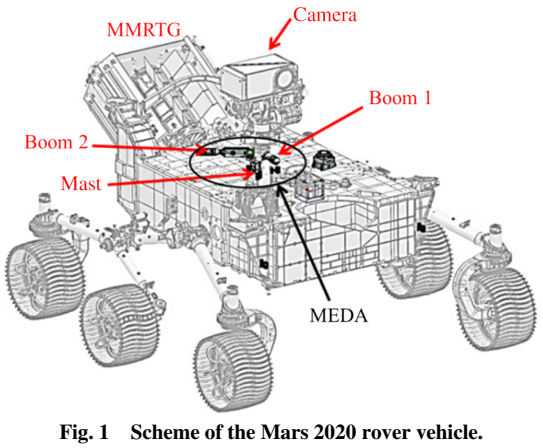

Fig. 1 Scheme of the Mars 2020 rover vehicle.

III. Experimental Setup

The Mars 2020 Rover experiments have been conducted in a low-speed tunnel at the National Institute of Aerospace Technology. More specifically, a closed return wind tunnel with an open elliptical test section of 2×3 m^2 has been used. This wind tunnel is capable of reaching a maximum airspeed of 60 m/s, and its freestream turbulence intensity is lower than 0.5%. Moreover, in order to simulate a flat planetary surface and study the flow in the desired horizontal plane, a vertical wooden platform has been installed in the wind tunnel to support the one-fifth-scaled Martian rover model studied. The model was made of plastic and built by additive manufacturing techniques (see Fig. 2), and it was placed on a circular plate that allowed the rotation axis to be aligned with the mast shaft axis.

Airflow around the scaled rover model was experimentally studied by means of particle image velocimetry, which is a nonintrusive quantitative flow measurement technique capable of obtaining the instantaneous two-dimensional flow velocity field [20–22].

To obtain an illuminated flowfield for PIV, the flow needed to be seeded with tracer particles. For this purpose, olive oil and an aerosol generator based on Laskin nozzles were used [23,24], effectively producing 1-μm-diameter tracer particles. The flow was then illuminated by two Neodymium-doped yttrium aluminium garnet lasers, delivering the maximum energy output of 190 mJ per pulse with a pulse separation time between them of 50 μs. To get clear and sharp images of particle positions, the pulse duration was 10 ns.

The illuminated flowfield containing the olive oil tracer particles was recorded by one charge-coupled device camera equipped with a Nikkon 80–200 mm camera lens. A synchronizer was used in order to control the camera so that the photographs could be taken simultaneously with the laser pulses. The resulting photographs had a resolution of 2048×2048 pixels, and the field of view (FOV) of the camera was 505×505 mm^2. The data acquisition rate of the PIV images was 10 Hz.

The averaged displacement of the particles was calculated by means of a cross-correlation analysis of the photographs acquired by the camera, which was implemented via a two-dimensional fast Fourier transform. The calculation is based on the particles contained within certain regions of the image known as interrogation windows [25]. Image processing of the results was then performed by following the Nyquist sampling criteria. To this effect, interrogation windows of 32×32 pixels with a 50% window overlap were used. The correlation peak was located by fitting a Gaussian curve with subpixel accuracy. A total of 100 instantaneous maps was acquired for every test that was carried out and then averaged out after postprocessing in order to obtain a set of mean flow velocity fields around the rover.

Given that the laser pulses used to acquire the data created a vertical laser sheet relative to the wind-tunnel platform and the desired plane of study in which the flow velocity maps were to be taken was horizontal relative to the rover model, it was necessary to

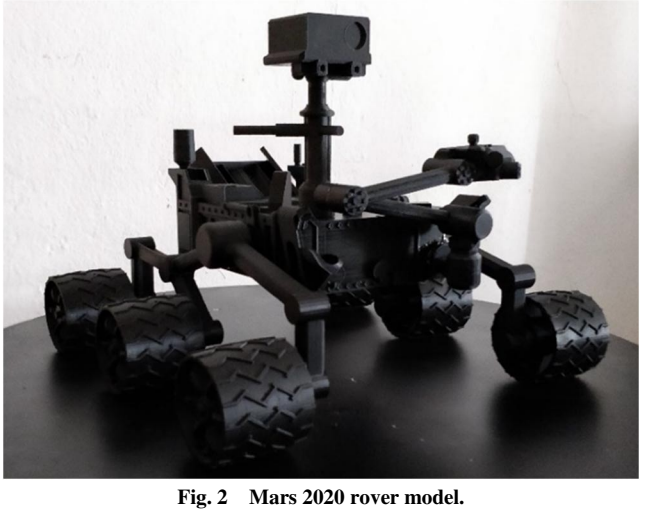

Fig. 2 Mars 2020 rover model.

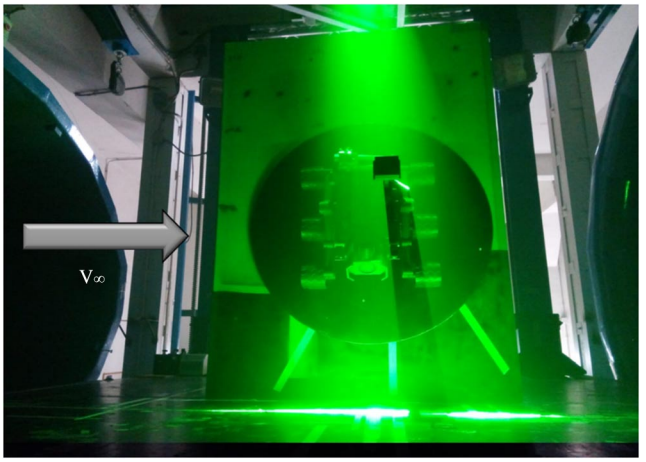

Fig. 3 Model of the Mars 2020 rover inside the wind-tunnel test section.

use an auxiliary wooden vertical wall to support the model (see Fig. 3) so that both planes overlapped.

Figure 3 shows the Mars 2020 Rover inside the wind-tunnel test section while being illuminated by one of the PIV laser pulses during one of the tests undertaken. As seen in the figure, shadow zones existed due to the rover model disrupting the laser sheet. Therefore, wherever the lighting is poor or inadequate, there will be windows of invalid data in the flow velocity fields. Additionally, due to the presence of certain components of the rover at approximately the same height as the wind sensors, and thus in close proximity to the laser sheet, overexposed regions will also be present from light scatter. This can be clearly seen in Fig. 4, in which the selected field of view and a PIV image are shown.

As a result, tracer particles will not be clearly detected on those regions, leading to low-quality data that can be removed during postprocessing.

IV. Similarity Laws

Because the validation of experimental results in wind tunnels relies on similarity laws, there must exist geometric similarity between the full-scale rover and the scaled model. Therefore, the same length scale ratio λ_L between all geometric dimensions of both the scaled and full-scaled rovers is required, as given by the following expression:

$$\lambda_L = \frac{L_m}{L_{\text{fs}}} \tag{1}$$

where L_m and L_{fs} stand for the model and full-scale lengths, respectively. A length scale ratio of one-fifth was chosen to improve the quality and resolution of the results, as well as reduce flow blockage effects in the wind tunnel [26].

Kinematic and dynamic similarities between the model and the prototype were also needed. The former requires both to have the same velocity scale ratio λ_V at all points, as given by Eq. (2):

$$\lambda_V = \frac{V_m}{V_{\text{fs}}} \tag{2}$$

where V_m and V_{fs} represent the model and full-scale flow velocities, respectively.

Moreover, the same Reynolds number Re for both model and full-scale prototypes is required in order to satisfy the dynamic similarity. Therefore,

$$Re_m = Re_{\text{fs}} \tag{3}$$

The Reynolds number is related to kinematic viscosity, the flow velocity, and a characteristic lineal dimension of the body by the following expression:

$$Re = \frac{VL}{\nu} \tag{4}$$

Consequently, dynamic similarity of the model can be hard to attain in some cases, especially when using low length scale ratios, because a much higher-velocity scale ratio would be needed.

However, because of the differences in air density and viscosity between Earth's and Mars's atmospheres, and hence in kinematic viscosity, the condition given by Eq. (3) can be more easily met in this case. The kinematic viscosity ratio is given by the following expression:

$$\lambda_\nu = \frac{\nu_m}{\nu_{\text{fs}}} \tag{5}$$

Therefore, for the dynamic similarity of the model to be attained, the following relation between length, velocity, and kinematic viscosity ratios is found:

$$\lambda_\nu = \lambda_V \lambda_L \tag{6}$$

The kinematic viscosity ratio depends only on the fluid properties inside the wind tunnel [around the rover model (ν_m))] and inside the Mars atmosphere [the full-scale rover (ν_{fs})], and thus cannot be changed. Therefore, the length and velocity scale ratios must be adjusted according to the previous expression so that the condition given by Eq. (3) is met, and the predicted Reynolds number is obtained.

Given that the kinematic viscosity scale is around 0.05 and the selected length scale of the model is 0.2, the velocity scale ratio was 0.25, according to Eq. (6). Thus, assuming standard air conditions, the proper freestream velocity of the wind tunnel in order to attain dynamic similarity was approximately 10 m/s.

Accordingly, the experiments were carried out with a freestream velocity of 10 m/s. The environmental variables during the tests were averaged out, taking values of 947.6 hPa of barometric pressure and 26.6°C of temperature, thus giving a Reynolds number of 2.2×10^5.

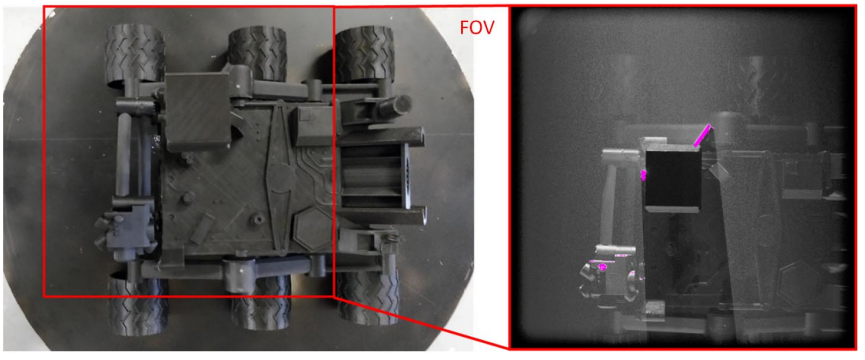

Fig. 4 Field of view (left) and photograph of the Mars 2020 rover model while being illuminated by the PIV laser sheet (right).

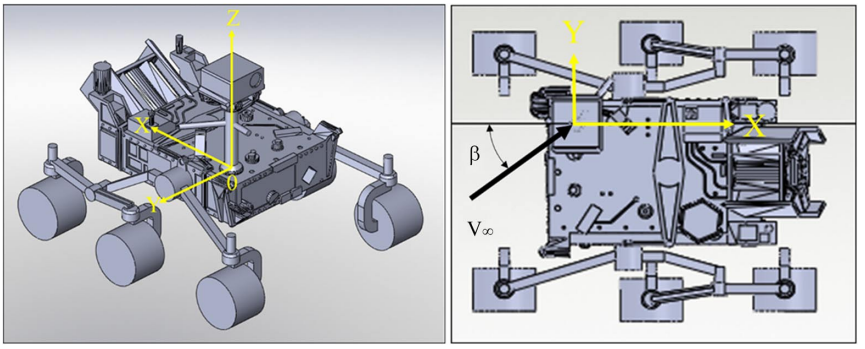

Fig. 5 Axes of the Mars 2020 rover (isometric and top views).

V. Description of the Experiments

A total of 12 different yaw angles (every 30 deg) of wind incidence relative to the model were studied in order to assess the influence of the rover body on the speed and direction of the wind measured by the MEDA of the rover. Looking at the design of the prototype shown in Fig. 1, this influence could be of some importance at certain angles because there are some components of the rover situated approximately at the same height of the wind sensors. The yaw angles and axes of the model were taken as shown in Fig. 5.

The Mars 2020 rover's MEDA system is supported by a vertical mast, in which the booms of the wind sensors are located, as shown in Fig. 6. There are two booms supporting the wind sensors; consequently, there will be active redundancy between them. The first one has a length of 170 mm and is placed toward the front of the model, whereas the second one is larger, with a length of 400 mm, and is rotated 120 deg clockwise relative to boom 1.

Sensors 1 and 2 will be located on the boom and will be known as S1 and S2, respectively. Both sensors are located at the end of each boom.

Because both booms were placed on the same horizontal plane, an assessment of the influence of one another on the measures was made in order to account for the interference between them. To this end, a total of four different configurations of the rover vertical mast were studied for each yaw angle, with the only difference between them being the wind sensor boom configuration, as depicted in Fig. 7.

Whereas configurations C0, C1, and C2 were studied to compare the measured flow velocity in both sensors S1 and S2, configuration C3 was included just for flow visualization purposes because it is the only one including both booms. This is due to the technique used to study the airflow around the model because it is not possible to know the flow velocity in the points corresponding to sensors S1 and S2 when its respective booms are included in the model.

Therefore, the only measurements taken into consideration for each sensor were the ones extracted from the mean flow velocity fields when its corresponding boom is not considered. The procedure to extract and compare the relevant data regarding airflow velocity as seen by the sensors is depicted in Fig. 8.

The flow velocity as would be seen by sensor S1 was measured in configurations C0 and C1, thus evaluating the interference from sensor S2 in the measurements taken by the former. The same applies in the case of sensor S2. The flow velocity as would be seen by sensor S2 were measured in configurations C0 and C2 in order for them to be compared.

VI. Results and Discussion

Flow velocity fields PIV maps around the Mars 2020 Rover model when both wind sensor booms were included (configuration C3) are first presented in Figs. 9 and 10 as dimensionless velocity maps for every yaw angle studied. This allows for a clear visualization of the flow around the model in each case, providing a preliminary assessment of the interference of the rover body, as well as the interference between booms. Streamlines of the airflow have been included on the flow velocity maps in order to further illustrate the flow direction around the wind sensors.

A displacement of the airflow is seen in Figs. 9 and 10 due to the presence of the robotic arm. The arm seems to alter the flow around sensor S1 at a yaw angle of 60 deg, hence altering the velocity measurement taken. Therefore, for a wind direction of 60 deg, there seems to be an interference between the robotic arm and the measurements of sensor S1. The wake downstream of the rear end of the

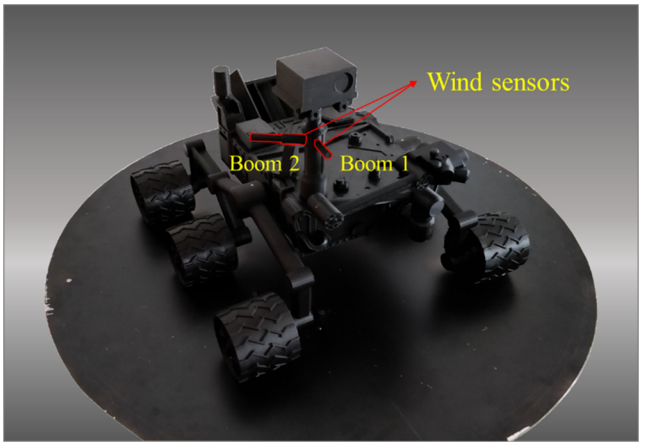

Fig. 6 Sketch of the 1:5-scaled rover with the wind sensors.

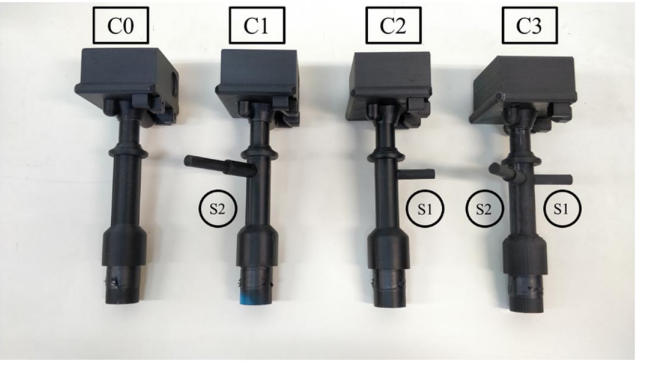

Fig. 7 Sketch of the rover mast configurations studied.

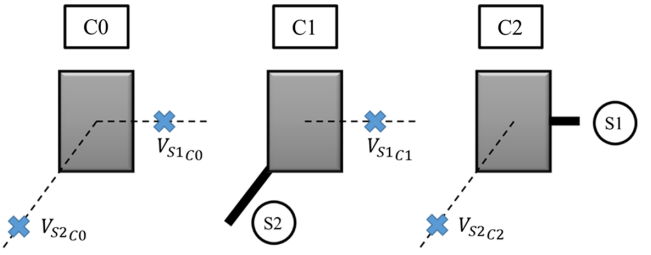

Fig. 8 Sketches of the data extracted from the tests.

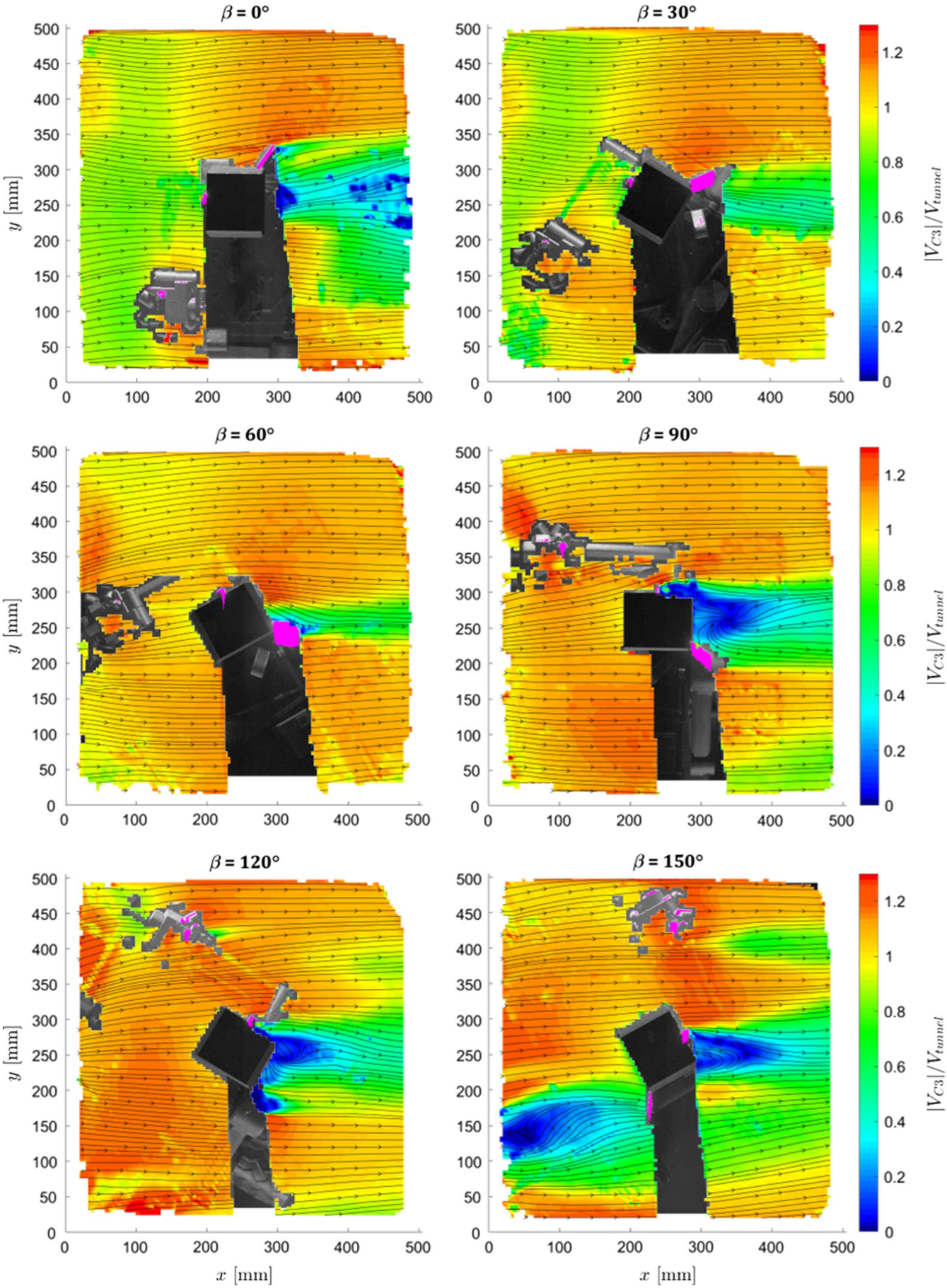

Fig. 9 Dimensionless flow velocity maps in configuration C3 with both sensors, with yaw angles from 0 to 150 deg.

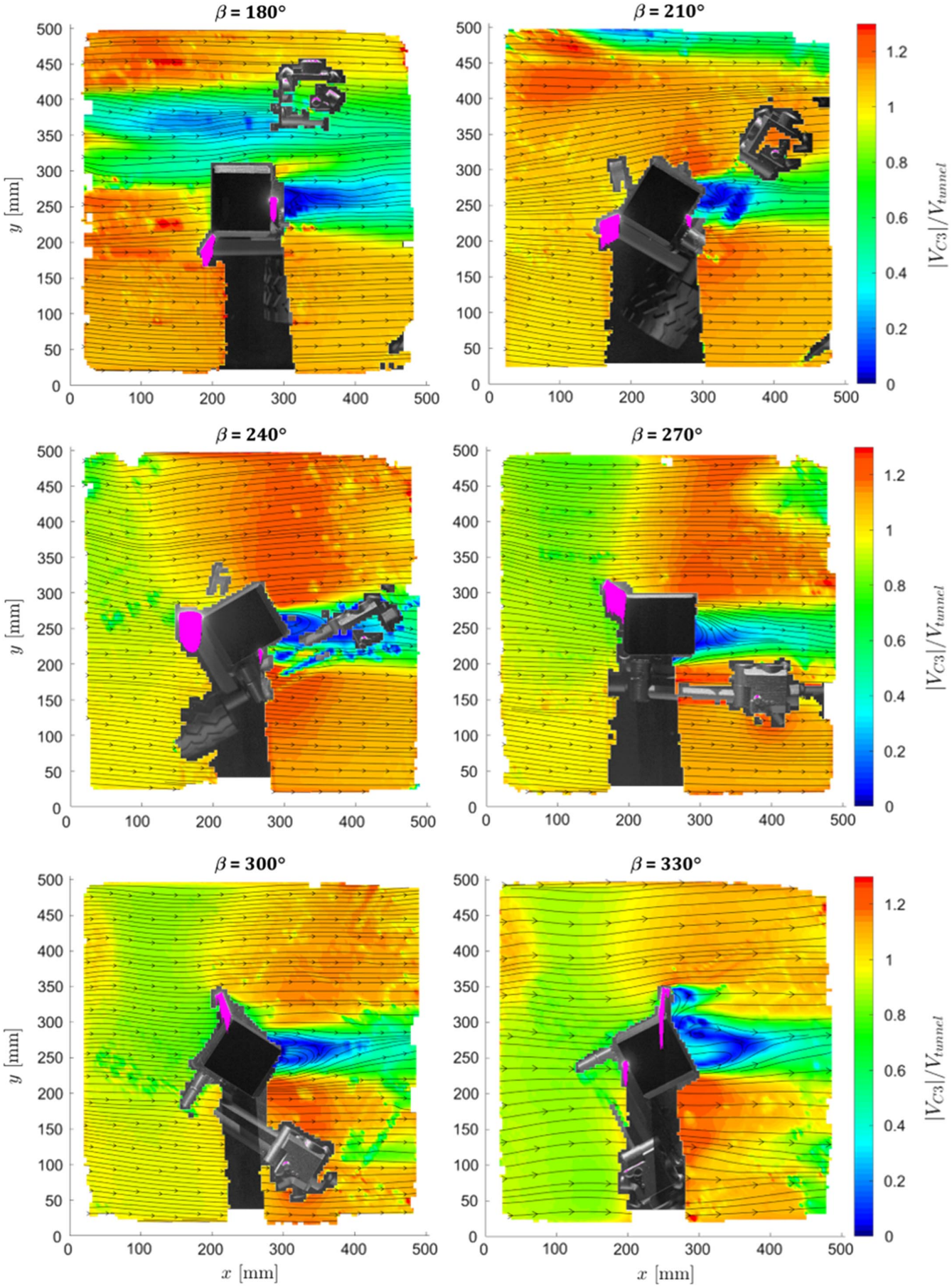

Fig. 10 Dimensionless flow velocity maps in configuration C3 with both sensors, with yaw angles from 180 to 330 deg.

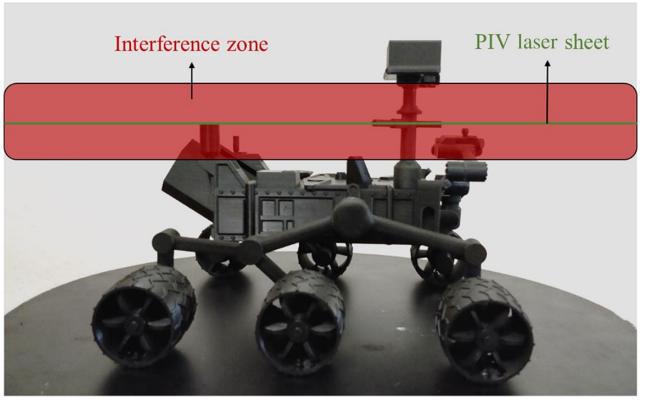

Fig. 11 Sketch of the rover model, the PIV laser sheet, and its interference zone.

rover can also be seen for a wind direction of 150, 180 and 210 deg, as well as the one downstream of the mast of the rover. Because the flows inside both wakes are fully detached, these will be regions where wind measurements from the sensors will not be accurate, and therefore should not be used. Because of this, given that one of the sensors will be in the mast wake for certain yaw angles, it is of the utmost importance that the other one is able to provide correct measurements. Figure 11 shows the height of the two main components of the Mars 2020 rover that interfere in the boom zone: the frontal articulated arm and the rear end of the rover, where the multimission radioisotope thermoelectric generator was located. The latter was out of the FOV of the tests undertaken. It can be observed that these two components were indeed near the horizontal plane that contains the booms. Both components modify the airflow around wind sensors, as observed in Figs. 9 and 10, thus compromising the measurements of the MEDA system.

The deflection of the airflow due to the presence of both booms is shown as well in both Figs. 9 and 10. As has already been suggested, because the flow deflection caused by one sensor can affect the wind measurement taken by the other, an evaluation of the interference was carried out by means of different mast configurations, as explained in Sec. VI (see the configurations in Figs. 7 and 8).

The results are summarized in Fig. 12 for both sensors S1 and S2 [on the left sensor (S1) and on the right sensor (S2)]. For sensor S1, dimensionless longitudinal and traversal velocity measurements are plotted versus the yaw angle at the location of sensor S1 (without the sensor S1 boom) for both configurations C0 (without any booms) and C1 (with sensor S2 boom). For sensor S2, an equivalent figure is obtained for configurations C0 (without any booms) and C2 (with sensor S1 boom).

For some wind angles, laser shadows lead to nonexistent points in Fig. 12. However, in the case of a yaw angle of 300 deg for sensor S1, although measurements for both configurations are displayed, sensor S2 produces a shadow; therefore, although configuration C0 produces a valid measurement, in configuration C1, it did not.

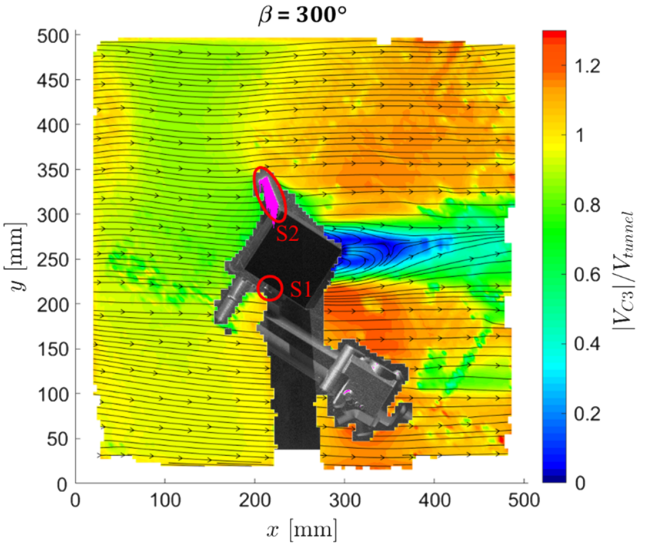

Fig. 13 Flow velocity for a wind direction of 150 deg in configuration C3.

Figure 13 illustrates this by overlapping flow velocity maps with the photograph of the rover model while illuminated by the laser sheet for the yaw angle 300 deg.

Figure 12 clearly shows the reduced magnitude in the $\tilde{u}$ velocity measurements of sensor S1 for wind directions of 150 and 180 deg, whereas for sensor S2, the reduced magnitudes are found for wind directions of 60 and 150 deg. Although the cavities detected in the $\tilde{u}$ velocity taken by sensors S1 and S2 at yaw angles of 180 and 60 deg, respectively, are to be expected due the mast wake, the one detected at 150 deg for sensor S2 requires further explanation. Similar figures to Fig. 13 are displayed in Figs. 14 and 15 for yaw angles of 60, 150, and 180 deg to better illustrate the location of the sensors in relation to the source of the cavities. It can be observed in Fig. 14 that, indeed, the invalid data in the velocity found at a yaw angle of 60 deg in sensor S2 and the cavities found at yaw angles of 180 and 150 deg in sensor S1 are due to the mast wake. It can also be observed that the reduced velocity magnitude for a yaw angle of 150 deg in sensor S2 is due to the wake of the MMRTG in the rear end of the rover.

Besides the wakes detected, the velocity measurements shown in Fig. 12 in both configurations are similar. To quantify the interference between the booms, the differences between the dimensionless velocities are plotted in Fig. 16 versus the yaw angle. The wind-tunnel airspeed was used as a reference to calculate the dimensionless velocities.

These differences in sensor data have been defined as follows:

$$\begin{cases} \Delta u_{S1} = u_{S1}^{C1} - u_{S1}^{C0} \\ \Delta u_{S2} = u_{S2}^{C2} - u_{S2}^{C0} \end{cases} \tag{7}$$

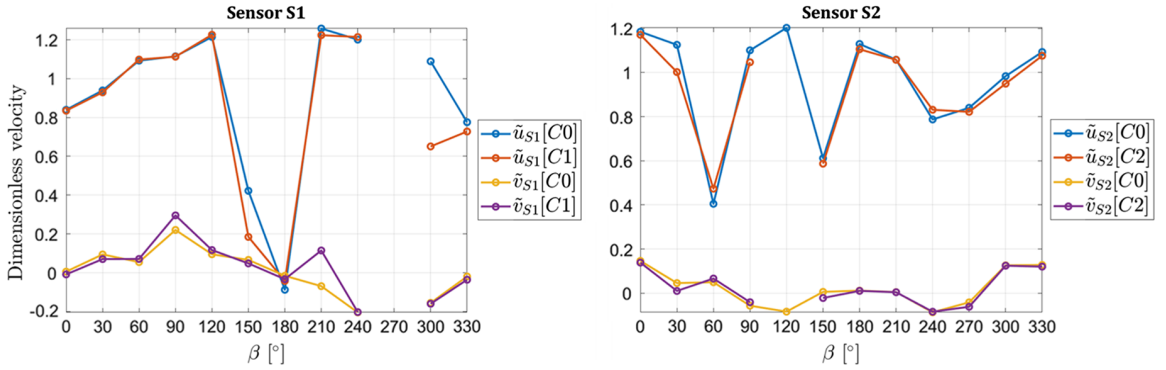

Fig. 12 Velocity measurements as seen by sensors S1 (left) and S2 (right), with and without the other one present.

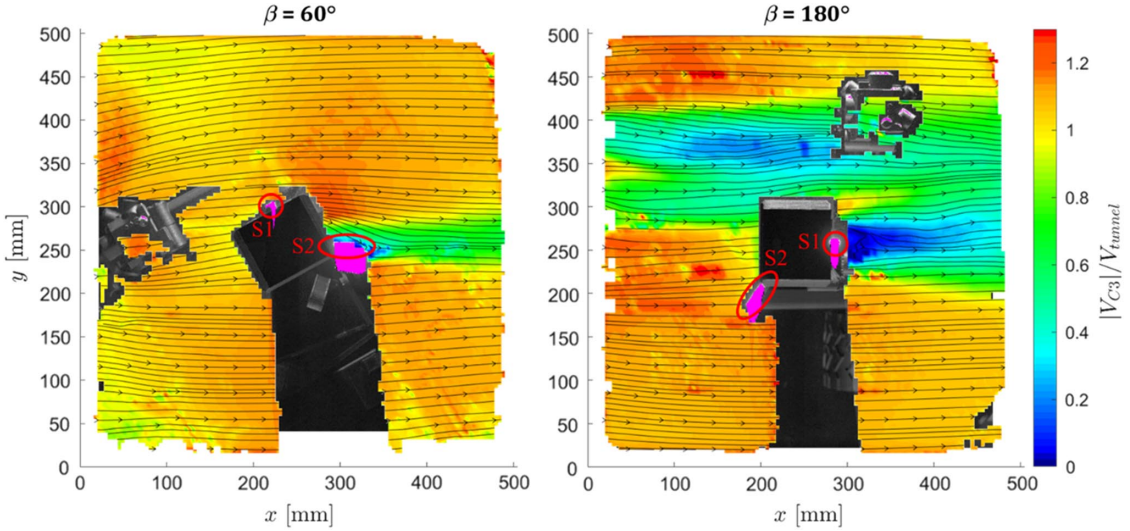

Fig. 14 Flow velocity maps for the wind directions in which sensors S2 (left) and S1 (right) are inside the mast wake in configuration C3.

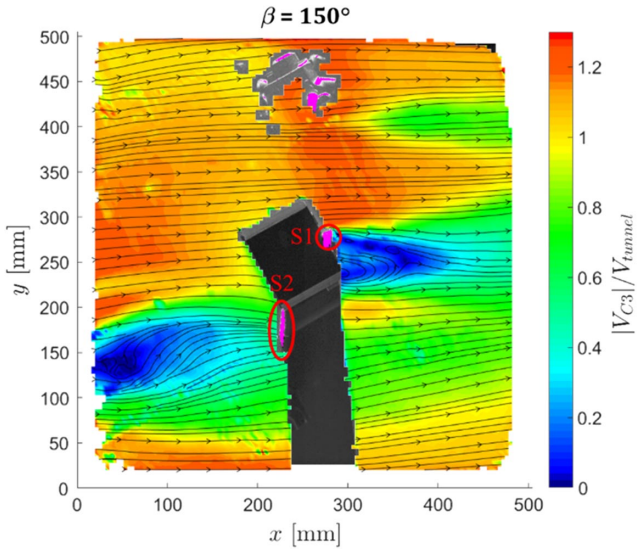

Fig. 15 Flow velocity for a wind direction of 150 deg in configuration C3.

where the subscript refers to the location of the velocity measurement (either sensor S1 or sensor S2), and the superscript is referring to the configuration (whether C0, C1, or C2).

For example, u_{S1}^{C1} would be the u component of the velocity taken as would be seen by sensor S1 using configuration C1 of the mast.

Looking at the relative difference depicted in Fig. 16, overall, it can be seen that the relative difference is indeed small because it is on the order of 3% of the freestream velocity. However, there are certain wind directions in which the relative difference is considerably larger and cannot be neglected.

For sensor S1, large differences are encountered at yaw angles of 90, 150, 180, and 210 deg. The relative error at a wind direction of 300 deg is due to its corresponding boom being located in the border of the shadow region, and is therefore to be considered as a spurious point. The larger errors are found at a wind direction of 150 deg, on account of sensor S1 being in the wake downstream of the mast, and for a yaw angle of 210 deg, due to the fact that sensor S1 is in the wake downstream of both the mast and boom 2. Both differences are approximately 20% of the freestream velocity. A similar figure to Fig. 13 is depicted in Fig. 17 for a yaw angle of 210 deg, showing that sensor S1 is inside the wake produced by sensor S2. For sensor S2, the larger differences shown in Fig. 16 are on the order of 10% of the freestream velocity and occur for yaw angles of 30 and 60 deg when sensor S2 is in the wake downstream of boom 1 and the mast, respectively. Because the length of sensor S2 is twice the length of sensor S1, its influence on the airflow will also be greater. The interference between the MEDA booms is clearly seen in Fig. 17, where the more representative flow velocity maps concerning that interference have been represented.

Finally, the last two figures summarize the results. First, the modulus of the velocity measured at each sensor for each angle is plotted in a radial plot in Fig. 18. Then, Fig. 19 summarizes the interference effect between the two booms (S1 and S2), the mast, the robotic arm, and the MMRGT explained throughout this section.

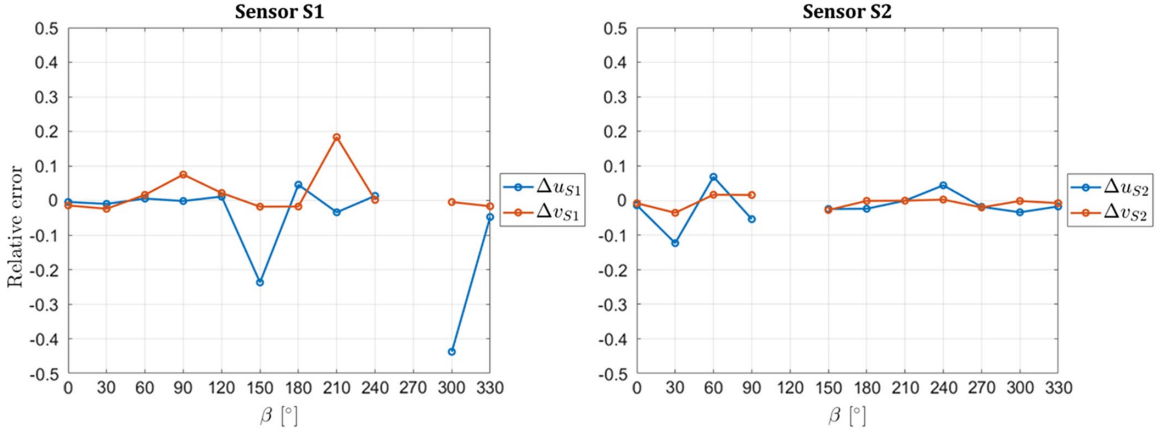

Fig. 16 Relative error between velocity measurements as seen by sensors S1 (left) and S2 (right) with and without the other one present.

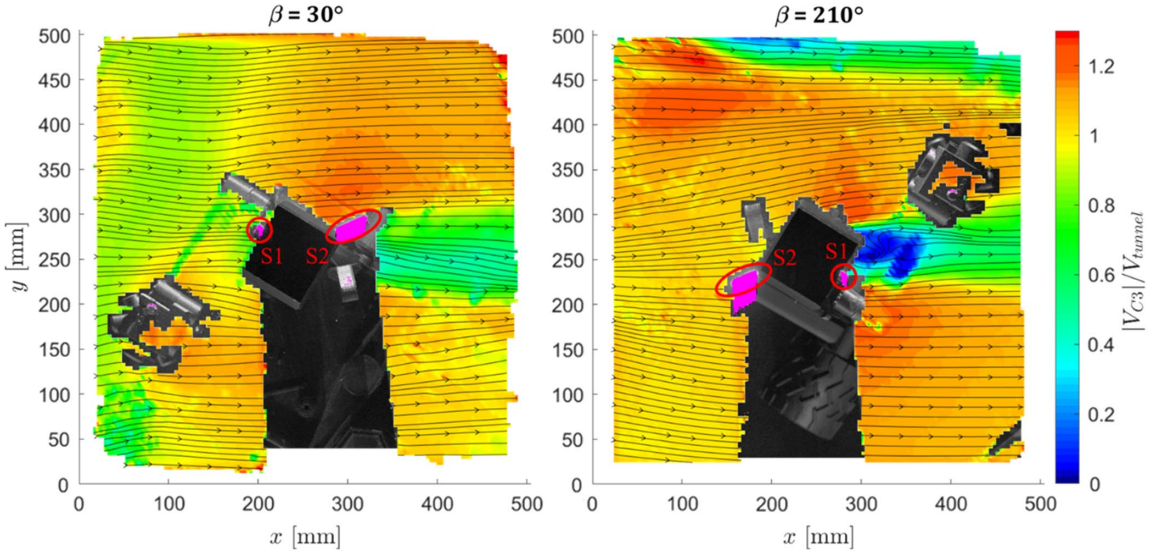

Fig. 17 Flow velocity maps for the wind directions in which sensors S2 (left) and S1 (right) are affected by the presence of the other boom in configuration C3.

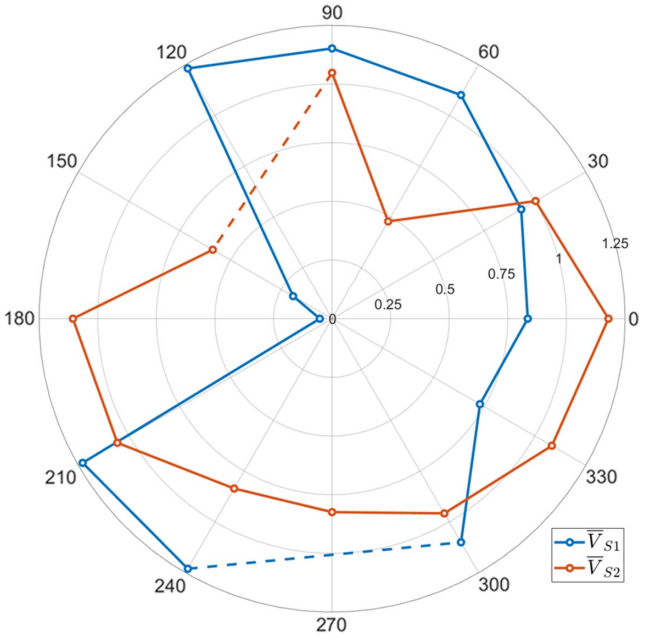

Fig. 18 Flow velocity radial maps at each sensor when the other boom is present.

VII. Conclusions

The flowfield around the wind sensor booms in the Mars 2020 rover has been investigated by PIV measurements of the horizontal plane that intersect both booms for 12 different yaw angles at the highest Reynolds number expected on Mars (2.2×10^5). The interference between the booms has been assessed by also testing different mast configurations with and without booms.

The PIV measurements have been presented, showing the importance of the wakes generated both by the camera mast (to which the booms are attached) and the MMRTG at the rear of the rover. It has also been found that the robotic arm influences the streamlines of the flowfield as well. Special attention should be given to these elements of the rover when studying its influence on the wind measurements.

The interferences between both booms have been evaluated and shown to be important at wind incidence angles of 210 and 30 deg for sensors S1 and S2, respectively. For those angles, the influence of boom 1 in sensor S2 is on the order of 10% of the freestream velocity, whereas the influence of boom 2 in sensor S1 is on the order of 20% of the freestream velocity.

The greater interference created by boom 2 with respect to the one created by boom 1 is due to its larger length. Therefore, it can be concluded that interference effects between booms should be taken into account if an accuracy of over 80% is required.

A significant interference between the rear end of the body of the rover and the wind measures taken by the MEDA system has also

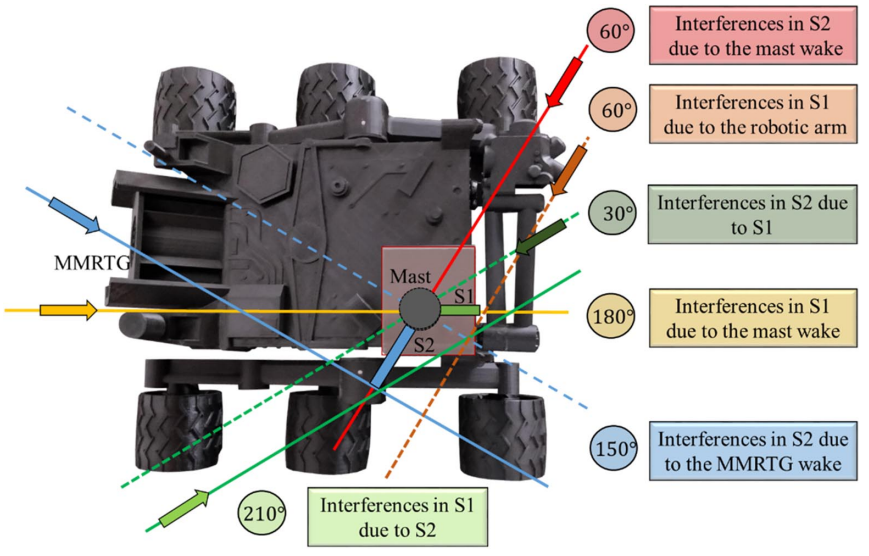

Fig. 19 Summary figure of the interferences.

been found at a yaw angle of 150 deg, creating a cavity in the velocity measured by sensor S2 that should be taken into account when analyzing the wind data.

Acknowledgment

This research has been supported under the Spanish National Institute of Aerospace Technology's internal project titled "Termo-fluidodinámica."

References

[1] Balme, M., and Greeley, R., "Dust Devils on Earth and Mars," *Reviews of Geophysics*, Vol. 44, No. 3, 2006, p. 2005RG000188. https://doi.org/10.1029/2005RG000188

[2] Lorenz, R. D., "Heuristic Estimation of Dust Devil Vortex Parameters and Trajectories from Single-Station Meteorological Observations: Application to in Sight at Mars," *Icarus*, Vol. 271, June 2016, pp. 326–337. https://doi.org/10.1016/j.icarus.2016.02.001

[3] Hueso, R., Ordonez-Etxeberria, I., and Sanchez-Lavega, A., "Martian Dust Devils: Paving the Way for Analysis of Pressure and Wind Data from MEDA on Mars 2020," *From Mars Express to ExoMars*, ESAC, Madrid, Spain, Feb. 2018, https://www.cosmos.esa.int/documents/1499429/1583871/Hueso_R.pdf.

[4] Day, M., Anderson, W., Kocurek, G., and Mohrig, D., "Carving Intracrater Layered Deposits with Wind on Mars," *Geophysical Research Letters*, Vol. 43, No. 6, 2016, pp. 2473–2479. https://doi.org/10.1002/grl.v43.6

[5] Hansen, C., Diniega, S., Bridges, N., Byrne, S., Dundas, C., Mcewen, A., and Portyankina, G., "Agents of Change on Mars' Northern Dunes: CO2 Ice and Wind," *Icarus*, Vol. 251, May 2015, pp. 264–274. https://doi.org/10.1016/j.icarus.2014.11.015

[6] Sullivan, R., Arvidson, R., Bell, J. F., Gellert, R., Golombek, M., Greeley, R., Herkenhoff, K., Johnson, J., Thompson, S., and Whelley, P., and Wray, J., "Wind-Driven Particle Mobility on Mars: Insights from Mars Exploration Rover Observations at 'El Dorado' and Surroundings at Gusev Crater," *Journal of Geophysical Research: Planets*, Vol. 113, No. E6, 2008. https://doi.org/10.1029/2008 JE003101

[7] Greeley, R., et al., "Gusev Crater: Wind-Related Features and Processes Observed by the Mars Exploration Rover Spirit," *Journal of Geophysical Research: Planets*, Vol. 111, No. E2, Jan. 2006, Paper E02S09. https://doi.org/10.1029/2005 JE002491

[8] Bridges, N. T., and Ehlmann, B. L., "The Mars Science Laboratory (MSL) Bagnold Dunes Campaign, Phase I: Overview and Introduction to the Special Issue," *Journal of Geophysical Research: Planets*, Vol. 123, Jan. 2018, pp. 3–19. https://doi.org/10.1002/2017 JE005401

[9] Hajos, G., Jones, J., Behar, A., and Dodd, M., "An Overview of Wind-Driven Rovers for Planetary Exploration," *43rd AIAA Aerospace Sciences Meeting and Exhibit*, AIAA Paper 2005-0244, Jan. 2005. https://doi.org/10.2514/6.2005-244

[10] Chamberlain, T. E., "Atmospheric Measurements on Mars: The Viking Meteorology Experiment," *Bulletin American Meteorological Society*, Vol. 57, No. 9, Sept. 1976, pp. 1094–1104. https://doi.org/10.1175/1520-0477(1976)057<1094:AMOMTV>2.0.CO;2

[11] Hess, S. L., Henry, R. M., Kuettner, J., Leovy, C. B., and Ryan, J. A., "Meteorology Experiments: The Viking Mars Lander," *Icarus*, Vol. 16, No. 1, 1972, pp. 196–204. https://doi.org/10.1016/0019-1035(72)90146-7

[12] Greene, G. C., Keafer, L. S., Jr., Marple, C. G., and Foughner, J. T., Jr., "Flow-Field Measurements Around a Mars Lander Model Using Hot-Film Anemometers Under Simulated Mars Surface Conditions," NASA TN D-6820, Sept. 1972.

[13] Seiff, A., Tillman, J. E., Murphy, J. R., Schofield, J. T., Crisp, D., Barnes, J. R., LaBaw, C., Mahoney, C., Mihalov, J. D., and Wilson, G. R., et al., "The Atmosphere Structure and Meteorology Instrument on the Mars Pathfinder Lander," *Journal of Geophysical Research*, Vol. 102, No. E2, Feb. 1997, pp. 4045–4056.

[14] Domínguez, M., Jiménez, V., Ricart, J., Kowalski, L., Torres, J., Navarro, S., Romeral, J., and Castañer, L., "A Hot Film Anemometer for the Martian Atmosphere," *Planetary and Space Science*, Elsevier, New York, 2008.

[15] Gómez-Elvira, J., Armiens, C., Castañer, L., Domínguez, M., Genzer, M., Gómez, F., Haberle, R., Harri, A. M., Jiménez, V., and Kahanpää, H., et al., "REMS: The Environmental Sensor Suite for the Mars Science Laboratory Rover," *Space Science Reviews*, Vol. 170, Nos. 1–4, 2012, pp. 583–640. https://doi.org/10.1007/s11214-012-9921-1

[16] Viúdez-Moreiras, D., Gómez-Elvira, J., Newman, C., Navarro, S., Marin, M., Torres, J., and Torre-Juárez, M. D. L., "Gale Surface Wind Characterization Based on the Mars Science Laboratory REMS Dataset. Part I: Wind Retrieval and Gales Wind Speeds and Directions," *Icarus*, Vol. 319, Feb. 2019, pp. 909–925. https://doi.org/10.1016/j.icarus.2018.10.011

[17] Gómez-Elvira, J., "Environmental Monitoring Instrument for Mars Exploration," *39th Lunar and Planetary Science Conference (Lunar and Planetary Science XXXIX)*, League City, Texas, March 2008, p. 1647.

[18] Bardera, R., Garcia-Magariño, A., Sor, S., and Urdiales, M., "Mars 2020 Rover Influence on Wind Measurements at Low Reynolds Number," *Journal of Spacecraft and Rockets*, Vol. 56, No. 4, 2019, pp. 1–7. https://doi.org/10.2514/1.A34362

[19] Bardera, R., Sor, S., Garcia-Magariño, A., Gómez-Elvira, J., Marin, M., Navarro, S., Torres, J., and Carretero, S., "Experimental and Numerical Characterization of the Flow Around the Mars 2020 Rover," *Journal of Spacecraft and Rockets*, Vol. 55, No. 5, 2018, pp. 1136–1143. https://doi.org/10.2514/1.A34217

[20] Raffel, M., Willert, C.E., Wereley, S. T., and Kompenhans, J., *Particle Image Velocimetry: A Practical Guide*, Springer, New York, 2007, pp. 3–12.

[21] Kompenhans, J., Raffel, M., and Willert, M., "PIV Applied to Aerodynamic Investigations in Wind Tunnels," VKI Lectures Series 1996-03, von Kármán Inst. For Fluid Dynamics, Rhode Saint Genese, Belgium, June 1996, https://elib.dlr.de/37494/.

[22] Adrian, R. J., and Westerweel, J., *Particle Image Velocimetry*, Cambridge Univ. Press, Cambridge, England, U.K., 2011, pp. 5–29.

[23] Echols, W.H., and Young, Y.A., "Studies of Portable Air-Operated Aerosol Generator," Naval Research Lab. Rept. 5929, Washington, D.C., 1963.

[24] Kähler, C. J., Sammler, B., and Kompenhans, J., "Generation and Control of Tracer Particles for Optical Flow Investigation in Air," *Experiments in Fluids*, Vol. 33, No. 6, 2002, pp. 736–742. https://doi.org/10.1007/s00348-002-0492-x

[25] Prasad, A. K., "Particle Image Velocimetry," *Current Science*, Vol. 79, No. 1, 2000, p. 10.

[26] Barlow, J. B., Rae, W. H., Jr., and Pope, A., *Low-Speed Wind Tunnel Testing*, 3rd ed., Wiley, New York, 1999, p. 656.

K. T. Edquist
Associate Editor